The Astrophysical Journal, 979:30 (13pp), 2025 January 20 https://doi.org/10.3847/1538-4357/ad98ee

Exploring Simple-population and Multiple-population Globular Clusters in the Outer Galactic Halo Using the Hubble Space Telescope

E. P. Lagioia[1], A. P. Milone[2,3], M. V. Legnardi[2], G. Cordoni[4], E. Dondoglio[3], A. Renzini[3], M. Tailo[3], T. Ziliotto[2], M. Carlos[5], S. Jang[6], A. F. Marino[3], A. Mohandasan[2], J. Qi[1], G. Rangwal[1], E. Bortolan[2], and F. Muratore[2]

[1] South-Western Institute for Astronomy Research Yunnan University, Kunming, 650500, People's Republic of China; elagioia@ynu.edu.cn
[2] Dipartimento di Fisica e Astronomia "Galileo Galilei," Università di Padova, Vicolo dell'Osservatorio 3, 35122, Padova, Italy
[3] Istituto Nazionale di Astrofisica—Osservatorio Astronomico di Padova, Vicolo dell'Osservatorio, 5, 35122, Padova, Italy
[4] Research School of Astronomy and Astrophysics, Australian National University, Canberra, ACT 2611, Australia
[5] Theoretical Astrophysics, Department of Physics and Astronomy, Uppsala University, Box 516, SE-751 20 Uppsala, Sweden
[6] Center for Galaxy Evolution Research and Department of Astronomy, Yonsei University, Seoul 03722, Republic of Korea

Received 2024 June 24; revised 2024 November 26; accepted 2024 November 26; published 2025 January 15

Abstract

The pseudo two-color diagram, known as chromosome map (ChM), is a valuable tool for identifying globular clusters (GCs), which consist of single or multiple stellar populations (MPs). Recent surveys of Galactic GCs using ChMs have provided stringent observational constraints on the formation of GCs and their stellar populations. However, these surveys have primarily focused on GCs at moderate distances from the Galactic center and composed of MPs. In this paper, we present the first detailed study of the stellar composition of four GCs in the outer halo of the Milky Way: Arp 2, Ruprecht 106, Terzan 7, and Terzan 8. Our analysis is based on high-precision photometry obtained from images collected with the Hubble Space Telescope in the F275W, F336W, F438W, F606W, and F814W bands. We find that Ruprecht 106 and Terzan 7 are composed solely of a single stellar population, whereas Arp 2 and Terzan 8 host both first- and second-population stars. In these clusters, the second population comprises about half and one-third of the total number of GC stars, respectively. The results from this paper and the literature suggest that the threshold in the initial GC mass, if present, should be smaller than approximately $10^5\,M_\odot$. The first-population stars of Arp 2 and Terzan 8, along with the stars of the simple-population GCs Ruprecht 106 and Terzan 7, exhibit intrinsic F275W – F814W color spreads, likely indicative of [Fe/H] variations of approximately 0.05–0.30 dex. This suggests that star-to-star metallicity variations are a common feature of star clusters, regardless of the presence of MPs.

Unified Astronomy Thesaurus concepts: Globular star clusters (656); Milky Way stellar halo (1060); Stellar populations (1622); Stellar abundances (1577); Ultraviolet astronomy (1736)

1. Introduction

In most Galactic globular clusters (GCs), stars exhibit variations in helium and light elements (see R. P. Kraft 1994; R. G. Gratton et al. 2012; N. Bastian & C. Lardo 2018; A. P. Milone & A. F. Marino 2022, for reviews). In particular, the abundance of C and N, O and Na, and Mg and Al show a negative pairwise correlation. Thus, N-rich stars are depleted in C and O, and enriched in He and Na. In fewer cases N-rich stars are also Al-rich and depleted in Mg (e.g., A. F. Marino et al. 2008; E. Carretta et al. 2009).

Old stars rich in C, O, and Mg are also commonly observed in the Galactic halo field. It is for this reason that coeval GC stars with similar chemical composition are thought to be formed during the first star formation burst that followed the collapse of the giant molecular cloud from which their host cluster originated. This gives a rationale for calling them first-population (or 1P) stars.

On the other side, GC members enriched in He, N, Na, and Al are rarely detected among field stars. The chemical composition of these stars bear the footprints of hot proton-capture reactions triggered in the CNO, NeNa, and MgAl chains, which are activated at effective temperatures ($T_{\rm eff}$) $\gtrsim$ 75 MK (P. A. Denisenkov & S. N. Denisenkova 1989). As a consequence, they are called second-population (or 2P) stars, because short-lived 1P stars are regarded as the gas donors from which 2P stars formed. 2P stars can therefore be identified as a stellar generation subsequent to that of 1P stars (P. L. Cottrell & G. S. Da Costa 1981; F. D'Antona et al. 1983; D. Yong et al. 2005; P. A. Denissenkov & F. D. A. Hartwick 2014), or as 1P stars that incorporated material processed by massive stars through accretion or binary interaction (S. E. de Mink et al. 2009; N. Bastian et al. 2013; M. Krause et al. 2013; M. Gieles et al. 2018; A. Renzini et al. 2022). 2P stars can constitute the main stellar component of massive GCs with multiple stellar populations (MPs; S. L. Martell et al. 2011; A. P. Milone et al. 2020; E. Dondoglio et al. 2021; S. Jang et al. 2022) but they are infrequent in the field, so that halo stars with 2P-like chemistry are thought to be lost from GCs through tidal interaction with the Galaxy.

Attempting to identify a comprehensive mechanism for the formation of MPs or, in simpler terms, discerning the nature of the 1P donors encounters various observational constraints that are challenging to meet simultaneously (for an extensive discussion on the various MP formation models and their implications, see A. Renzini et al. 2015, 2022). Determining the relation between the properties of the MPs and the main parameters of the host cluster, such as the GC mass and the orbit, may provide constraints to the GC formation. To better refine our understanding of the formation scenarios, it is also crucial to ascertain whether MPs are a widespread trait among Galactic GCs or whether only clusters surpassing a specific mass threshold can sustain the formation of MPs.

Variations in abundance among stars contribute to a corresponding spread in colors in photometric diagrams obtained from specific filters (e.g., A. F. Marino et al. 2008; D. Yong & F. Grundahl 2008; A. P. Milone et al. 2012a; J.-W. Lee 2015; A. P. Milone & A. F. Marino 2022; V. J. Mehta et al. 2025, and references therein). As an example, a photometric diagram dubbed a chromosome map (ChM) is an efficient and widely used tool to disentangle 1P and 2P stars along the main sequence (MS), red giant branch (RGB), and asymptotic giant branch (AGB) of star clusters. A ChM is a pseudo two-color diagram typically constructed with the pseudo-color $C_{\rm F275W,F336W,F438W} = (m_{\rm F275W} - m_{\rm F336W}) - (m_{\rm F336W} - m_{\rm F814W})$, mainly sensitive to internal variations in C, N and O, and the color $m_{\rm F275W} - m_{\rm F814W}$, which improves the identification of stars with varying helium content (A. P. Milone et al. 2015; E. P. Lagioia et al. 2018, 2021; A. F. Marino et al. 2019a). Various photometric surveys of Galactic GCs based on ChMs (A. P. Milone et al. 2017; S. Jang et al. 2022) reveal the ubiquitous presence of MPs in all investigated clusters. These results support and reinforce similar conclusions drawn from spectroscopic analyses (R. Gratton et al. 2004; R. G. Gratton et al. 2012; A. F. Marino et al. 2019a).

In this context, the identification of simple-population (SP) GCs, namely clusters with chemically homogeneous stars, casts doubt on the universal occurrence of MPs, thus challenging the view of MPs as a phenomenon inherent to the protocluster environment. The best prototypes of SP GCs are Ruprecht 106 and Terzan 7. For the first cluster, spectroscopic analyses by S. Villanova et al. (2013), P. François (2014), and H. Frelijj et al. (2021) revealed homogeneous light-element abundances. Moreover, analysis of the cluster horizontal branch (HB) morphology by A. P. Milone et al. (2014), and photometry in the F336W, F438W, and F814W bands by A. Dotter et al. (2018) suggested that the color distribution of RGB stars was consistent with that of a single stellar population. Similarly, evidence based on ground-based *U*, *B*, *I* photometry that the star cluster Terzan 7 contains a single stellar population has been provided by E. P. Lagioia et al. (2019b).

Recently, we have been granted 62 orbits during Cycle 30 of the Hubble Space Telescope (HST; GO-17075, PI: Lagioia) to investigate for the first time the ChMs of four outer-halo clusters. The targets include Ruprecht 106 and Terzan 7, the two aforementioned candidate SP GCs, but which have never been studied through ChMs, which is mandatory for a conclusive assessment about either presence or absence of MPs. The other two targets are Arp 2 and Terzan 8.

The choice of our targets was based on the following criteria: Galactocentric distance, metallicity, mass, and origin. With respect to the first criterion, the Galactocentric distance of all the targets exceeds 15 kpc (W. E. Harris 1996, 2010 update; H. Baumgardt & E. Vasiliev 2021).

As for the metallicity, the selected clusters span a wide range of iron content, ranging from the metal-poor cluster Terzan 8 ($[\rm Fe/H] \simeq -2.3$ dex; M. Mottini et al. 2008; E. Carretta et al. 2014) to the subsolar-metallicity cluster Terzan 7 ($[\rm Fe/H] = -0.62$ dex; G. Tautvaišienė et al. 2004). We notice that the average metallicity values reported in the W. E. Harris (1996, 2010 update) catalog span a similar interval, with $[\rm Fe/H] = -2.18$ dex for Terzan 8 and $[\rm Fe/H] = -0.32$ dex for Terzan 7.

All the targets are relatively small clusters with present-day masses $M \leqslant 4 \times 10^4 M_\odot$, except Terzan 8, which is the most massive GC among them, with $M \sim 7.5 \times 10^4 M_\odot$ (H. Baumgardt & M. Hilker 2018, 2023 update). H. Baumgardt and collaborators have also provided an estimate of the initial mass of the target clusters,[7] $M_{\rm in}$, that for three out of four clusters is smaller (albeit marginally in the case of Ruprecht 106) than $\sim 1.5 \times 10^5 M_\odot$, a threshold value proposed by A. P. Milone et al. (2020) for the onset of MPs. It is worth mentioning that according to studies based on the analysis of the CN and CH indices in low-resolution spectra of relatively small and distant GCs, the initial mass threshold for the onset of MPs might be lower than the value suggested by A. P. Milone et al. (2020) and approximately equal to $2 \times 10^4 M_\odot$ (R. Salinas & J. Strader 2015; B. Tang et al. 2021; R. Huang et al. 2024).

Finally, concerning the last criterion, several studies indicate a probable ex situ genesis of Arp 2, Terzan 7, and Terzan 8, which are associated to the Sagittarius (Sgr) dwarf spheroidal galaxy (dSph; M. Bellazzini et al. 2003; D. R. Law & S. R. Majewski 2010; E. Carretta et al. 2014) and likely still bound to its main body (M. Bellazzini et al. 2020). The origin of Ruprecht 106 is doubtful: While previous studies rule out a link between this cluster and Sgr (e.g., B. J. Pritzl et al. 2005), recent kinematic studies instead assess its association to the Sgr stream (A. R. Shirazi et al. 2024). Interestingly, L. Sbordone et al. (2007) showed that the chemical composition of Ruprecht 106 is similar to that of the Sgr field stars. More recently, S. Villanova et al. (2013), P. François (2014), and F. Lucertini et al. (2023) have suggested an extragalactic origin for Ruprecht 106 based on the relative chemical abundance of $[\alpha/\rm Fe]$ and *r*- and *s*-process elements in the analyzed stars, compared to those typical of GC and field stars of similar metallicity.

The four target clusters represent, therefore, an ideal sample to study to which extent the environment affects the formation of MPs and to shed new light on the physical conditions driving the emergence of MPs. Table 1 reports the main parameters of the four GCs.

The outline of the paper includes Section 2, where we describe the data set and the data reduction techniques adopted in our analysis. Then, Section 3 presents UV-optical-NIR color–magnitude diagrams (CMDs) of the four targets clusters. In Section 4, we present the first ChMs of our GCs, while in Section 5 we investigate the metallicity of GC stars. Finally, the summary and the discussion are provided in Section 6.

2. Data Analysis

The observation data set analyzed in this work for Arp 2, Terzan 7, and Terzan 8 consists of images collected by HST with the Wide Field Camera 3 (WFC3) camera in the F275W,

---

[7] H. Baumgardt & M. Hilker (2018) provided advanced estimates for the initial masses of the Galactic GCs. Their determinations face several uncertainties which depend on our limited understanding of the evolutionary history of the Milky Way, and therefore of its tidal field. Other uncertainties are related to the knowledge of the primordial mass segregation in clusters and their early chemo-dynamical evolution, in particular the amount of mass lost through interaction with the molecular clouds from which they originated. We notice that the aforementioned GC initial mass estimates are obtained by assuming a time-independent Galactic gravitational potential and no initial mass segregation.

Table 1
Main Parameters of the Four Globular Clusters Analyzed in This Work

Cluster	$R_{\rm GC}$ (kpc)	[Fe/H] (dex)	$E(B-V)$ (mag)	M ($10^4\,M_\odot$)	$M_{\rm in}$ ($10^5\,M_\odot$)	$r_{\rm hl}$ (arcmin)	$v_{\rm esc}$ (km s^{-1})	Age (Gyr)
Arp 2	21.39	−1.75	0.10	3.87	0.912	1.70	4.5	13.00
Ruprecht 106	18.04	−1.68	0.20	3.40	1.259	1.26	5.6	11.50
Terzan 7	16.85	−0.32	0.07	2.23	0.525	0.90	4.6	8.00
Terzan 8	20.43	−2.16	0.12	7.59	7.586	1.89	6.0	13.50

Note. For our analysis, we adopted the average metallicity values from W. E. Harris (1996, 2010 update). The listed reddening values have been also taken from the same catalog. It is worth noting that M. Mottini et al. (2008) found [Fe/H] = −1.83 for Arp 2, while S. Villanova et al. (2013) obtained [Fe/H] = −1.47 for Ruprecht 106. Ages are taken from A. Dotter et al. (2010) except for Ruprecht 106, for which the age comes from A. Dotter et al. (2018). All other quantities listed in the table are derived from the 2023 updated version of the catalog of the Fundamental Parameters of Galactic Globular Clusters available at the following URL: https://people.smp.uq.edu.au/HolgerBaumgardt/globular/. Column (1): cluster ID. Column (2): Galactocentric distance. Column (3): iron content. Column (4): reddening. Columns (5) and (6): actual mass and initial mass, respectively. Column (7): half-light radius. Column (8): escape velocity. Column (9): age.

F336W, and F438W bands of the UVIS channel during Cycle 30 (GO-17075, PI: Lagioia), and of Advanced Camera for Surveys (ACS)/WFC images in the F606W and F814W bands of ACS/WFC, already present on the MAST archive before the execution of the GO-17075 program.[8] For Ruprecht 106, only F275W observations were collected during GO-17075, whereas the F336W and F438W images are available from the archive. The HST data collected for the GO-17075 and analyzed in this paper can be found in MAST doi:10.17909/23y6-1r51. Details on the exposures used in this works are outlined in Table 2.

The data reduction was performed with the software IMG2XYM (J. Anderson et al. 2006). The software takes as input the `flc` images, which are HST pipeline-calibrated individual exposures corrected for pixel-based charge transfer efficiency (J. Anderson & L. R. Bedin 2010). For each analyzed image, a 5 × 5 array of perturbed point-spread functions (PSFs) is generated starting from library empirical PSF models, and improved with spatial-variation corrections obtained from unsaturated and isolated bright stars. Saturated stars are also identified and their magnitude is accurately determined by taking into account the flux bled into adjacent pixels (J. Anderson et al. 2008; R. L. Gilliland et al. 2010).

Instrumental magnitudes were calibrated to the VEGA-MAG system using the method of L. R. Bedin et al. (2005), incorporating UVIS and WFC encircled energy distributions and photometric zero-points from the STScI website. Geometric distortion corrections were applied to star positions using the solution presented by A. Bellini et al. (2011), and the positions were transformed to the Gaia Data Release 3 reference system (Gaia Collaboration et al. 2023). Finally, we selected stars measured with high photometric accuracy, following the methodology outlined in A. P. Milone et al. (2009) which is based on the `q-fit`, a quality index provided by the software.

To determine the cluster membership for each target, we took advantage of the large temporal baseline of our observations and compute proper motions (PMs). The adopted method is based on the displacement of stars observed at different epochs with respect to the motion of a sample of reference stars. Since cluster members have a negligible PM dispersion compared to field stars, we referred the PMs to a sample of bright, unsaturated cluster stars that are well fitted by the PSF model. We refer to the papers by J. Anderson et al. (2006), E. P. Lagioia et al. (2014), and M. Tailo et al. (2021), and references therein for details on the procedure.

As shown by M. Tailo et al. (2021, their Figure 1), who derived the stellar PMs of stars in the fields of view studied in this paper by using the HST data available at that time, the field stars and the cluster members are well separated in the PM diagrams and the residual field contamination is negligible.

As a final step, we verified that the photometry of each cluster is not significantly affected by differential reddening. Hence, we corrected the photometry for the effects of spatial-dependent variation of the photometric zero-point, which are due to small inaccuracies in the PSF models, by applying the procedure outlined in A. P. Milone et al. (2012b).

Overall, the data set that we collected for analyzing MPs in our four outer-halo GCs is similar to that adopted in the recent surveys of Galactic GCs (G. Piotto et al. 2015; A. P. Milone et al. 2017), which are based on similar data in the F275W, F336W, F438W, F606W, and F814W bands of the WFC3/UVIS and ACS/WFC cameras of HST. Since we have derived stellar photometry and astrometry using the same methods and computer programs adopted in previous surveys, we can directly compare our results with former analyses focused on MPs in GCs, taking advantage of a sample composed by 62 Galactic GCs.

3. The UV-optical-NIR CMDs

The CMDs built with the $m_{\rm F275W} - m_{\rm F814W}$ and $C_{\rm F275W,F336W,F438W}$ color indices are efficient tools to detect MPs. To this end, we plot in Figure 1 the $m_{\rm F275W}$ versus $m_{\rm F275W} - m_{\rm F814W}$ CMDs of our four targets, from the most metal-poor (top left) to the most metal-rich (bottom right). In each panel, the error bars on the right side indicate the typical magnitude and photometric color error at the corresponding F275W magnitude.

We see that the faint region of each CMD is populated by MS stars reaching ∼1–2 mag below the turn-off (TO). We also observed conspicuous populations of blue stragglers and prominent sequences of MS-MS binary systems with large mass ratios, which appear on the red side of the MS in each cluster. The upper CMD region is populated by RGB, HB, and AGB stars. It is worth noticing the short color distribution of

---

[8] https://archive.stsci.edu/

HB stars in all the target GCs. While theoretical prescriptions imply that young and metal-rich GCs display short HBs, the same phenomenon observed in intermediate-metallicity GCs might serve as an indirect indication that there is negligible to no helium enhancement among the cluster stars, as in the case of Ruprecht 106 (A. P. Milone et al. 2014). Among the analyzed GCs, the most metal-poor targets Arp 2 and Terzan 8 display slightly more extended HBs ($\boldsymbol{\Delta}(m_{\rm F275W} - m_{\rm F814W}) \sim$ 1.5 mag).

Figure 2 displays the $m_{\rm F438W}$ versus $C_{\rm F275W,F336W,F438W}$ pseudo-CMDs of our targets, arranged as in Figure 1. The pseudo-CMDs of the two GCs in the top row show the largest color spread among the four targets. In particular, we observe a distinct split along the entire RGB extension in Arp 2, whereas the RGB stars of Terzan 8 with comparable magnitudes display a broad color spread, with indications of a split.

In both the cases, the $C_{\rm F275W,F336W,F438W}$ pseudo-color broadening of RGB stars is taken as evidence that these clusters harbor MPs. A spurious effect due to random errors in the pseudo-color is ruled out by the size of the color error bars. On the other side, the RGB spread visible in the CMDs of Ruprecht 106 and Terzan 7 is comparable with the error in color along the whole RGB extension. This suggests that Arp 2 and Terzan 8 harbor MPs with different light-element abundances, while Ruprecht 106 and Terzan 7 may not.

4. The Chromosome Maps

To further investigate the stellar populations along the RGB of the studied GCs, we constructed a pseudo-color–color diagram called a ChM. In this diagram, stars with different light-element contents such as helium, carbon, nitrogen, oxygen, and magnesium occupy specific regions (A. P. Milone et al. 2017; A. F. Marino et al. 2019b). As a result, a ChM grants the ability to classify large numbers of stars into various populations and with an accuracy which competes with that provided by high-resolution spectroscopy (A. F. Marino et al. 2019a). In the subsequent section, we briefly describe the method used to derive the ChMs of the studied GCs, whereas in Section 4.2 we present the analysis of the ChMs and results on the fraction of 1P and 2P stars in the target clusters.

4.1. Constructing the Chromosome Maps

A ChM displays along the abscissa and ordinate the indices $\Delta_{\rm F275W,F814W}$ and $\Delta C_{\rm F275W,F336W,F438W}$, respectively. Specific details on the procedure to derive a ChM have been widely discussed in various papers of our team (e.g., A. P. Milone et al. 2017; E. P. Lagioia et al. 2021), to which we refer the interested reader.

In a nutshell, to derive the ChM abscissa we take advantage of the $m_{\rm F814W}$ versus $m_{\rm F275W} - m_{\rm F814W}$ CMD, and of the $m_{\rm F814W}$ versus $C_{\rm F275W,F336W,F438W}$ pseudo-CMD to derive the ChM ordinate. In both these diagrams, we measure the (pseudo-) color displacement of every RGB star relative to the red boundary of the RGB sequence, and divide it by the broadening of the RGB sequence. The RGB broadening is defined as the (pseudo-) color difference between the red and the blue RGB boundaries at the same F814W star's magnitude. This result of this process, called verticalization, is a normalized color ratio that is finally multiplied by a factor called the intrinsic RGB width.

To derive the intrinsic RGB width, we first measure the broadening of the RGB, or observed RGB width, at a reference F814W magnitude, set by convention at $m^{\rm MSTO} - 2$.[9] Then, since the observed RGB width encompasses both the intrinsic RGB width and the observational error, it is necessary to estimate the contribution of the latter to the observed RGB width. To do that, we simulate the $m_{\rm F814W}$ versus $m_{\rm F275W} - m_{\rm F814W}$ and $m_{\rm F814W}$ versus $C_{\rm F275W,F336W,F438W}$ diagrams for a SP composed of 10,000 stars. The errors associated to each magnitude of the simulated stars are extracted from a Gaussian distribution with a dispersion corresponding to the median magnitude error of the RGB stars. Finally, the intrinsic RGB width in the color $m_{\rm F275W} - m_{\rm F814W}$ and in the pseudo-color $C_{\rm F275W,F336W,F438W}$, indicated respectively as $W_{\rm F275W,F814W}$ and $W_{C\,\rm F275W,F336W,F438W}$, are obtained by subtracting in quadrature the RGB widths of the simulated CMD from the observed RGB width ones.

To evaluate the statistical error affecting our determination of $W_{\rm F275W,F814W}$ and $W_{C\rm F275W,F336W,F438W}$, we applied a bootstrapping test with replacement 1000 times to the observed RGB colors and magnitudes. For each system configuration, we measured the intrinsic RGB width. We calculated the median value of the 1000 RGB-width determinations, and the residuals from the median. We assumed that the 68th percentile of the distribution of the absolute values of the residuals corresponds to the uncertainty associated to the intrinsic RGB widths $W_{\rm F275W,F814W}$ and $W_{C\rm F275W,F336W,F438W}$. The values of the intrinsic width and the statistical error for the four targets GCs are reported in Table 3.

The estimates of the RGB width of our target GCs allow us to contextualize these four clusters within the broader trend of absolute chemical variations observed in previously studied Galactic GCs (A. P. Milone et al. 2017; E. P. Lagioia et al. 2019a). For this purpose, Figure 3 shows the intrinsic $W_{C\,\rm F275W,F336W,F438W}$ as a function of the average iron abundance for the 58 Galactic GCs studied by A. P. Milone et al. (2018b, gray dots) and the four outer-halo GCs studied in this paper (colored symbols). We find that Terzan 8 and Arp 2 follow the $W_{C\,\rm F275W,F336W,F438W}$–[Fe/H] correlation of the bulk of studied GCs. On the other hand, Ruprecht 106 and Terzan 7 are remarkable exceptions, having RGB widths smaller than those of GCs at similar metallicities. This observation supports the indication from the color extension in the $m_{\rm F814W}$ versus $C_{\rm F275W,F336W,F438W}$ pseudo-CMD in Figure 2 that the two latter clusters may not host MPs. In this regard a definitive conclusion is provided in the next section,

---

[9] The F814W luminosity of the MSTO has been determined by using the naive estimator method (B. W. Silverman 1986). First, we selected a magnitude interval in the $m_{\rm F814W}$ versus $m_{\rm F438W} - m_{\rm F814W}$ CMD which includes MS and sub-giant branch stars, and divided it into a given number of magnitude bins. Then, we computed the median color and magnitude of the stars in each bin. The whole procedure was repeated n times, with n assuming a different value for each cluster ($n = 5, 6, 8$), keeping the bin width unchanged but shifting the starting point of the first bin by an amount equivalent to $1/n$th of the bin width. For each bin, the resulting median points have been linearly interpolated across the entire initial magnitude interval, thus obtaining a raw fiducial line, which has been finally smoothed by boxcar-averaging three adjacent points. Finally, the magnitude of the bluest point of the smoothed fiducial line has been taken as the cluster MSTO luminosity in the F814W band. A similar approach has been adopted for the determination of the RGB boundaries. The blue and red RGB envelopes correspond, respectively, to the fiducial lines interpolating the 4th and 96th percentiles of the RGB (pseudo-) color distribution in each bin, across the whole magnitude range covered by the cluster RGB members. Their relative distance at two F814W magnitudes above the MSTO corresponds to the observed RGB width.

Table 2
Data Set of HST Observations Analyzed in This Work

Cluster	Date (DD/MM/YY)	Camera/Channel	Filter	$N \times$ Exposure Time (s)	Proposal ID (PI Last Name)
Arp 2	2023 Mar 6–17	WFC3/UVIS	F275W	25×1325	17075 (Lagioia)
	2023 Apr 25–26	WFC3/UVIS	F275W	2×1325	17075 (Lagioia)
	2023 Mar 12–17	WFC3/UVIS	F336W	11×795	17075 (Lagioia)
	2023 Mar 12–17	WFC3/UVIS	F438W	11×348	17075 (Lagioia)
	2016 May 3	ACS/WFC	F606W	$45 + 2 \times (554 + 555) + 4 \times 556$	14235 (Sohn)
	2006 Apr 22	ACS/WFC	F606W	$40 + 5 \times 345$	10775 (Sarajedini)
	2006 Apr 22	ACS/WFC	F814W	$40 + 5 \times 345$	10775 (Sarajedini)
Ruprecht 106	2023 Jun 29–30	WFC3/UVIS	F275W	$2 \times (1401 + 1402)$	17075 (Lagioia)
	2023 Jul 7–12	WFC3/UVIS	F275W	$12 \times (1401 + 1402)$	17075 (Lagioia)
	2010 Dec 10	WFC3/UVIS	F336W	2×1100	14726 (Dotter)
	2017 Mar 29	WFC3/UVIS	F336W	2×1100	14726 (Dotter)
	2017 May 30–31	WFC3/UVIS	F336W	2×1100	14726 (Dotter)
	2017 Sep 29	WFC3/UVIS	F336W	4×1100	14726 (Dotter)
	2016 Dec 10	WFC3/UVIS	F438W	571	14726 (Dotter)
	2017 Mar 29	WFC3/UVIS	F438W	571	14726 (Dotter)
	2017 May 31	WFC3/UVIS	F438W	571	14726 (Dotter)
	2017 Sep 21	WFC3/UVIS	F438W	2×571	14726 (Dotter)
	2010 Jul 4	ACS/WFC	F606W	$55 + 4 \times 550$	11586 (Dotter)
	2016 Jul 12	ACS/WFC	F606W	$60 + 841 + 844 + 2 \times (842 + 845)$	14235 (Sohn)
	2010 Jul 4	ACS/WFC	F814W	$60 + 3 \times 585 + 586$	11586 (Dotter)
Terzan 7	2023 Mar 8–16	WFC3/UVIS	F275W	17×1325	17075 (Lagioia)
	2023 Mar 14–15	WFC3/UVIS	F336W	$3 \times 795 + 837 + 2 \times 838$	17075 (Lagioia)
	2023 Mar 14	WFC3/UVIS	F438W	3×348	17075 (Lagioia)
	2006 Jun 3	ACS/WFC	F606W	$40 + 5 \times 345$	10775 (Sarajedini)
	2016 May 4	ACS/WFC	F606W	$45 + 2 \times (554 + 555) + 4 \times 556$	14235 (Sohn)
	2006 Jun 3	ACS/WFC	F814W	$40 + 5 \times 345$	10775 (Sarajedini)
Terzan 8	2023 Mar 9–23	WFC3/UVIS	F275W	9×1325	17075 (Lagioia)
	2023 Apr 18–30	WFC3/UVIS	F275W	15×1325	17075 (Lagioia)
	2023 May 1	WFC3/UVIS	F275W	1325	17075 (Lagioia)
	2023 Mar 16	WFC3/UVIS	F336W	795	17075 (Lagioia)
	2023 Apr 24–30	WFC3/UVIS	F336W	9×795	17075 (Lagioia)
	2023 May 1	WFC3/UVIS	F336W	795	17075 (Lagioia)
	2023 Mar 16	WFC3/UVIS	F438W	348	17075 (Lagioia)
	2023 Apr 24–30	WFC3/UVIS	F438W	9×348	17075 (Lagioia)
	2023 May 1	WFC3/UVIS	F438W	348	17075 (Lagioia)
	2006 Jun 3	ACS/WFC	F606W	$40 + 5 \times 345$	10775 (Sarajedini)
	2016 Apr 28	ACS/WFC	F606W	$45 + 2 \times (554 + 555) + 4 \times 556$	14325 (Sohn)
	2006 Jun 3	ACS/WFC	F814W	$40 + 5 \times 345$	10775 (Sarajedini)

where the detailed stellar composition of the target clusters is explored through the ChM.

4.2. Multiple Stellar Populations in the Chromosome Map

As mentioned in the beginning of Section 4, a ChM allows us to tag the different stellar populations in a GC. As an example, in Figure 4, we illustrate the procedure to select the 1P and 2P stars of the outer-halo GC Arp 2. In the left panel of the figure, we plot the $\Delta C_{\rm F275W,F336W,F438W}$ versus $\Delta_{\rm F275W,F814W}$ ChM of the RGB members of the cluster (gray points).

The orange points in the bottom-left corner display the photometric errors of the ChM. Their elliptical distribution spans few tenths of magnitudes in both the horizontal and vertical directions, thus indicating that the spread across the ChM is intrinsic. The choice to artificially plot the error distribution on the bottom-left side, so that its median along the y-axis corresponds to $\Delta C_{\rm F275W,F336W,F438W} = 0$, is instrumental to the illustration of the procedure for selecting 1P stars and deriving their relative fraction.

The study of the ChM of 58 GCs by A. P. Milone et al. (2017) has shown that 1P stars cluster around the origin of the ChM, whereas the 2P stars define a sequence that extends toward larger absolute values of $\Delta C_{\rm F275W,F336W,F438W}$ and $\Delta_{\rm F275W,F814W}$ (A. P. Milone et al. 2017). For the sake of representation, we overplot a dotted–dashed line on the ChM with an inclination of 18° to the negative direction of the x-axis. This line represents the typical inclination of the bulk of 1P stars in the ChM (A. P. Milone et al. 2017, their Figure 2) and has been used to fix the rotation angle of the ChM in the middle panel. Here, both the ChM and the error distribution have been rotated counterclockwise by 18°, so that the dotted–dashed line is now parallel to the x-axis. The rotated system, with abscissa and ordinate $\Delta'_{\rm F275W,F814W}$ and $\Delta' C_{\rm F275W,F336W,F438W}$,

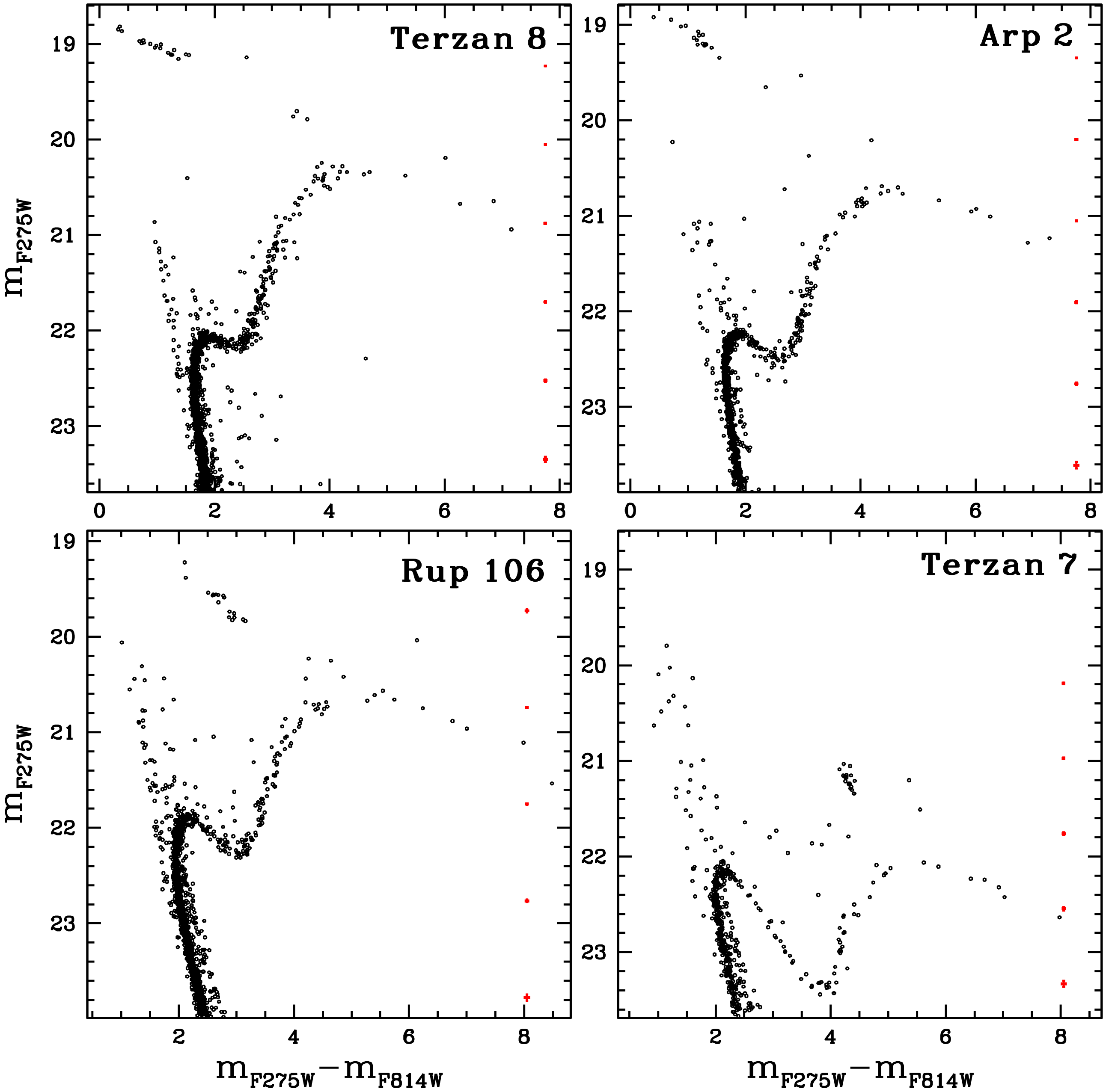

Figure 1. $m_{\rm F275W}$ vs. $m_{\rm F275W} - m_{\rm F814W}$ CMDs of the four clusters analyzed in this work, arranged by increasing metallicity from left to right and top to bottom. In each panel, the vertical and horizontal error bars on the right-hand side represent the typical magnitude and color errors at different F275W magnitudes.

respectively, allows us to identify the candidate 1P and 2P cluster stars and estimate the fraction of 1P stars with respect to the total number of RGB stars.

To do this, we plot in the right panel the histogram distributions of the $\Delta' C_{\rm F275W,F336W,F438W}$ values (gray-filled histogram) and of the errors (orange histogram). We see that the ChM histogram shows a bimodal distribution, with the bottom one associated to the 1P stars, and the top one to the 2P stars. This evidence demonstrates that Arp 2 is not chemically homogeneous.

Therefore, we calculated the 95th percentile of the error distribution along the *y*-axis (dotted line in the middle panel). This line delimits the portion of the ChM histogram that we have used to least-squares fit a first-guess Gaussian to the 1P histogram distribution. Then, we performed a new Gaussian fit but limited to the portion of the histogram with $\Delta' C_{\rm F275W,F336W,F438W}$ smaller than twice the dispersion of the first-guess Gaussian. Finally, we used the red dashed line, corresponding to the peak of the best-fit Gaussian function (red curve in the right panel) shifted by twice the Gaussian dispersion, to identify the groups of bona fide 1P and 2P stars. Finally, the ratio between the area of the best-fit Gaussian and the total area of the ChM histogram has been taken as the fraction of 1P cluster stars. In the case of Arp 2, we find $N_{\rm 1P}/N_{\rm TOT} = 0.533 \pm 0.052$.

We applied the same procedure to build the ChM, select the candidate 1P and 2P stars, and determine the corresponding $N_{\rm 1P}/N_{\rm TOT}$ for the other three target clusters.

The ChMs of the four target GCs are shown in Figure 5, where we display in the bottom-right corner the corresponding photometric error distributions (orange dots). We note that in the case of Terzan 8, Arp 2, and Ruprecht 106, the horizontal

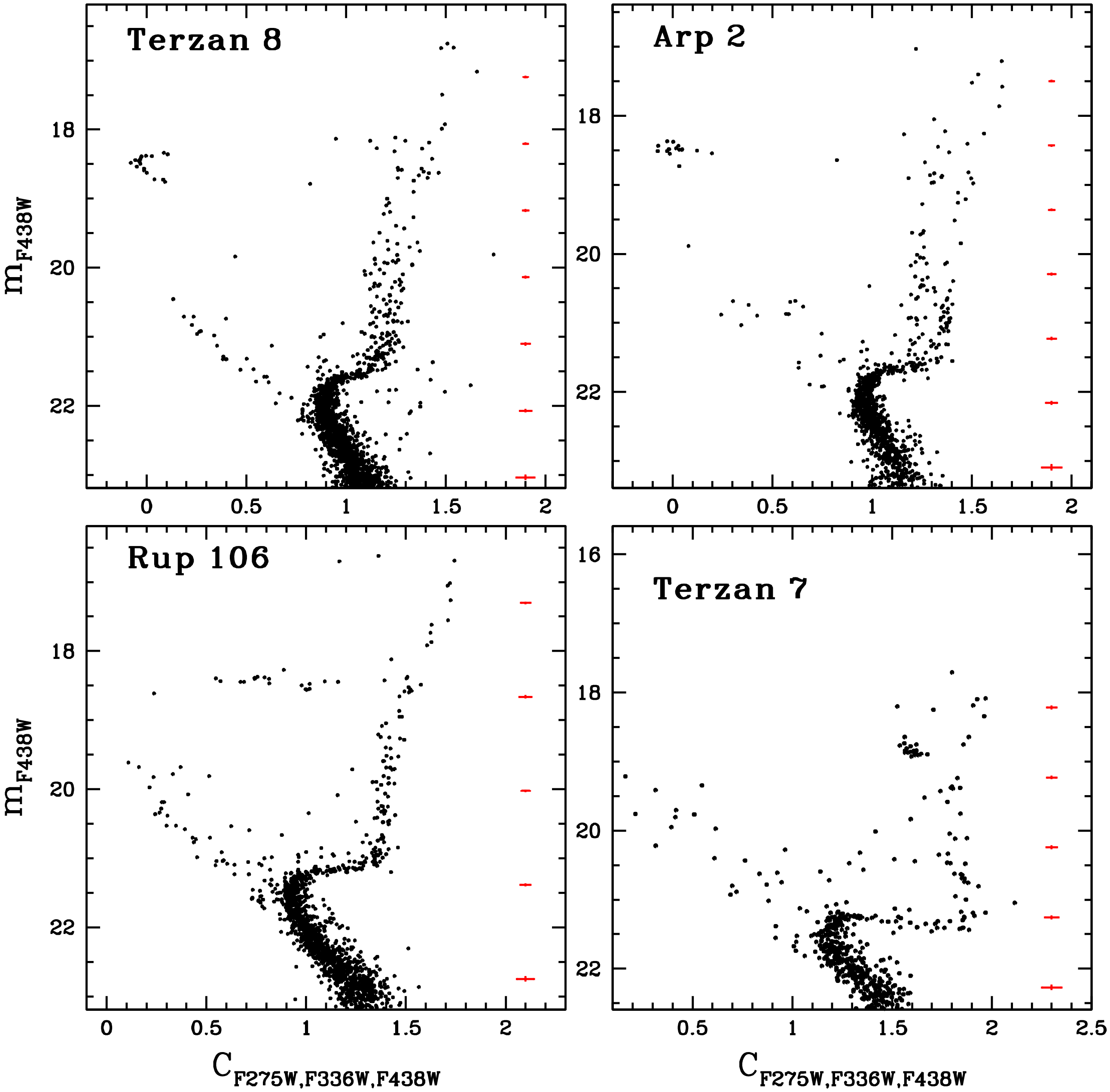

Figure 2. m_{F438W} vs. $C_{F275W,F336W,F438W}$ pseudo-CMDs of the four target clusters, arranged as in Figure 1. In each panel, the error bars on the right side indicate the typical color and magnitude errors at different F438W magnitudes.

and vertical extension of their ChMs is much larger than that of the photometric error distribution. However, in Terzan 7, both the horizontal and vertical spread of the ChM is comparable to those of the photometric error. These impressions are also confirmed by the density diagrams displayed in the inset of each panel, where the gray-shaded areas represent the density of the observed ChM points, and the orange-shaded area refers to the error distribution.

Similar to Figure 4, the red dashed line in the ChMs of Terzan 8 and Arp 2 separates bona fide 1P and 2P stars. As far as Ruprecht 106 and Terzan 7 are concerned, our procedure results in a homogeneous composition of 1P stars only. Both Terzan 8 and Arp 2 show a relatively high fraction of 1P stars compared to most of the studied Galactic GCs. In particular, in Terzan 8, ~71% of the cluster RGB stars belong to the 1P fraction, thus making it one of the Galactic GCs with the largest fractions of 1P stars. The 1P predominance in this cluster, identified as a 1P-dominated GC by V. Caloi & F. D'Antona (2011) based on the analysis of its HB morphology, aligns partially with the spectroscopic findings of E. Carretta et al. (2014). E. Carretta et al. (2014) estimated the 2P fraction in Terzan 8 to be approximately 6%, with only one out of the 16 analyzed stars showing an Na abundance consistent with 2P stars. The discrepancy between this study's estimated 2P fraction ($N_{2P}/N_{TOT} \sim 29\%$) and the value reported by E. Carretta et al. (2014) likely arises from the smaller sample size used in the latter analysis. Finally, in the case of Arp 2, 1P stars make up a fraction slightly larger than 50% of the RGB cluster stars.

Given the moderate population of 53 RGB stars in Terzan 7, we conducted Monte Carlo tests to estimate the probability of detecting zero 2P stars if their fraction ranges from 1% to 10%.

Table 3
Values of the RGB Widths, Fraction of 1P Candidate Stars, Total Number of Stars Analyzed in the Chromosome Map, and Maximum Radial Distance from the Cluster Center ($r_{\rm max}$) as a Fraction of the Cluster Half-light Radius ($r_{\rm hl}$)

Cluster	$W_{\rm F275W,F814W}$ (mag)	$W_{C\,\rm F275W,F336W,F438W}$ (mag)	$N_{\rm 1P}/N_{\rm TOT}$	$N_{\rm TOT}$	$r_{\rm max}/r_{\rm hl}$
Arp 2	0.111 ± 0.096	0.196 ± 0.024	0.533 ± 0.052	96	0.98
Ruprecht 106	0.125 ± 0.006	0.100 ± 0.020	1.000 ± 0.010	109	1.25
Terzan 7	0.152 ± 0.051	0.081 ± 0.015	1.000 ± 0.020	53	1.66
Terzan 8	0.203 ± 0.021	0.188 ± 0.024	0.705 ± 0.044	114	0.84

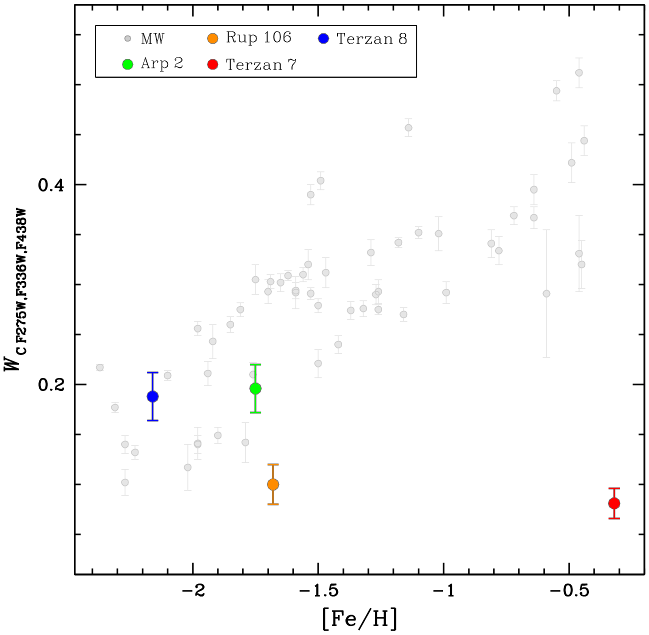

Figure 3. RGB width in the pseudo-color $C_{\rm F275W,F336W,F438W}$ as a function of iron abundance. The gray points represent the 58 MW clusters analyzed in A. P. Milone et al. (2018a). The four target clusters studied in this paper are represented as colored points, as reported in the inset.

We found that if 2P stars make up 2% of the total number of stars, the probability of detecting zero 2P stars in a sample of 53 stars is approximately 68%. Similarly, for Ruprecht 106, which has 109 RGB stars, the fraction of 2P stars that results in a 68% probability of zero detections is about 1%. Therefore, we considered 0.02 and 0.01 as our estimate of the uncertainty associated with the fraction of 2P stars in Terzan 7 and Ruprecht 106.

The fractions of 1P stars, the total number of RGB stars in the ChM of each target cluster, as well as their maximum radial distance as a function of the corresponding cluster half-light radius are reported in Table 3.

Figure 6 shows the fraction of 1P stars as a function of the logarithm of the present-day and initial GC mass (left and middle panel, respectively) and the GC escape velocity (right panel). In addition to the GCs studied in this paper, the GC sample comprises the Galactic (gray circles) and Magellanic Cloud star clusters (gray triangles) homogeneously analyzed by using the ChMs (A. P. Milone et al. 2017, 2020; E. Dondoglio et al. 2021).

Terzan 8 and Arp 2 follow the same trend as the other Galactic GCs, thus corroborating the evidence of the anticorrelation between the fraction of 1P stars and both cluster mass and escape velocity. The MP GC with the smallest initial mass, Arp 2, has $M_{\rm in} \lesssim 10^5\,M_\odot$, which is slightly lower than the empirical mass threshold of $\sim 1.5 \times 10^5\,M_\odot$ suggested by A. P. Milone et al. (2020) as the limit for the occurrence of MPs. In the same work, Milone and collaborators showed that the Large and Small Magellanic Clouds also host SP GCs with initial masses larger than the proposed threshold.

Our results therefore represent the first photometric evidence based on the distribution of RGB stars in the ChM of the existence of SP clusters, namely Ruprecht 106 and Terzan 7. At the same time we provide the first photometric evidence that MPs are present in the GCs Terzan 8 and Arp 2.

5. Metallicity Variations among First-population Stars

A visual inspection of the ChMs of Figure 5 reveals that the 1P stars of all clusters span a wider $\Delta_{\rm F275W,F814W}$ range than that expected from the observational uncertainties alone.

In particular, we note that, although Ruprecht 106 does not show any vertical spread, so no presence of 2P stars, the horizontal extension of its ChM covers a $\Delta_{\rm F275W,F814W}$ interval of $\sim$0.25 mag, significantly wider than that of the photometric errors. Such a phenomenon is even more pronounced in the case of Terzan 8, where the extension of the 1P candidate stars is $\sim$0.3 mag, while in the case of Arp 2 1P and 2P stars seem to span a comparable interval along the x-axis.

Recent works have shown that the horizontal width of 1P stars in the ChMs is a widespread phenomenon among Galactic GCs, and demonstrated that 1P stars are not chemically homogeneous (A. P. Milone et al. 2015, 2018b; F. D'Antona et al. 2016). Papers based on both spectroscopy and photometry have shown that the $\Delta_{\rm F275W,F814W}$ range of 1P stars is mostly due to metallicity variations (e.g., A. F. Marino et al. 2019a, 2023; M. V. Legnardi et al. 2022). It is important to emphasize that, while additional spectroscopic analyses are needed to confirm the presence of a metallicity spread in every GC with an extended 1P sequence, alternative explanations have been proposed to account for the observed elongation of 1P stars. These alternatives include variations in helium content and the presence of unresolved interacting binaries among evolved stars, such as blue stragglers and red giants. However, the observational properties of these stars in the CMD cannot fully account for the spread observed among 1P stars in the ChM (A. F. Marino et al. 2019b, 2023; S. Kamann et al. 2020; F. Martins et al. 2020; C. Lardo et al. 2022; M. V. Legnardi et al. 2022).

To quantify the metallicity variations among the 1P stars of the studied clusters, we followed the method of M. V. Legnardi et al. (2022, 2024). Briefly, we first determined the $\Delta_{\rm F275W,F814W}$ extension of the 1P sequence as the difference between the 90th and the 10th percentiles of the $\Delta_{\rm F275W,F814W}$ distribution. The intrinsic width, $W^{\rm 1G}_{\rm F275W,F814W}$, was estimated by subtracting the color errors in quadrature. Assuming that the observed color spread on the ChM solely derives from metallicity variations, we

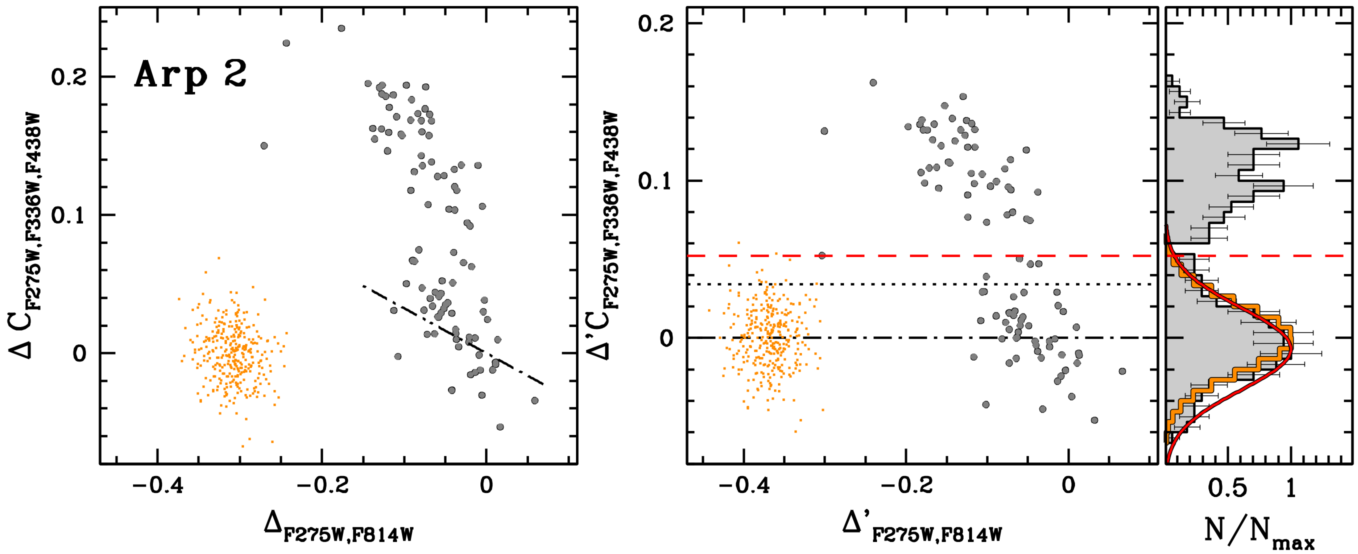

Figure 4. Procedure for the selection of the candidate 1P and 2P stars of Arp 2. Left panel: $\Delta C_{\rm F275W,F336W,F438W}$ vs. $\Delta_{\rm F275W,F814W}$ ChM of the cluster RGB stars (gray points). The orange dots represent the photometric error distribution of the ChM. The dotted–dashed line marks the inclination of 1P stars with respect to the *x*-axis and has a value of 18°. Middle panel: ChM and error distribution rotated counterclockwise by an angle of 18°. In the rotated reference system $\Delta' C_{\rm F275W,F336W,F438W}$ vs. Δ′F275W, F814W, the dotted–dashed line is parallel to the *x*-axis. The dotted line marks the 95th percentile of the photometric error distribution along the *y*-axis. Right panel: vertical histogram distribution of the ChM (gray-filled area) and photometric errors (orange histogram). The red curve represents the best-fit Gaussian to the region of the histogram delimited by the dotted line (see text for explanation). The red dashed line is the vertical coordinate corresponding to twice the dispersion of the best-fit Gaussian above its peak, and marks the separation between bona fide 1P and 2P cluster stars.

used the relation between the $m_{\rm F275W} - m_{\rm F814W}$ color and metallicity by A. Dotter et al. (2008) to convert the $W^{\rm 1G}_{\rm F275W,F814W}$ values into [Fe/H] variations. Among the investigated targets, Terzan 8 exhibits the highest [Fe/H] spread ($\delta[{\rm Fe/H}]^{\rm MAX}_{\rm 1G} = 0.373 \pm 0.060$), while Terzan 7 displays the lowest value ($\delta[{\rm Fe/H}]^{\rm MAX}_{\rm 1G} = 0.036 \pm 0.010$). Arp 2 and Ruprecht 106 show moderate [Fe/H] variations, with $\delta[{\rm Fe/H}]^{\rm MAX}_{\rm 1G} = 0.087 \pm 0.014$ and 0.120 ± 0.011, respectively.

In the left panel of Figure 7, we present the maximum iron variation among 1P stars plotted against the logarithm of the cluster mass (H. Baumgardt & M. Hilker 2018, 2023 update) and iron abundance (W. E. Harris 1996, 2010 update). The gray dots represent the 55 Galactic GCs investigated by M. V. Legnardi et al. (2022), whereas the colored symbols indicate the four targets examined in this study. The SP clusters studied by M. V. Legnardi et al. (2024), namely NGC 6791 and NGC 1783, are represented with a square and a triangle, respectively.

Our results corroborate the evidence of a mild correlation between $\delta[{\rm Fe/H}]_{\rm MAX}^{\rm 1G}$ and the metallicity, and between $\delta[{\rm Fe/H}]_{\rm MAX}^{\rm 1G}$ and mass. Indeed, the $\delta[{\rm Fe/H}]^{\rm MAX}_{\rm 1G}$ values obtained for Arp 2, Ruprecht 106, and Terzan 7 follow the general trend in both the diagrams. Conversely, 1P stars in Terzan 8 exhibit higher metallicity variations compared to Galactic GCs with similar mass/metallicity.

Moreover, the evidence of extended 1P sequences in the ChMs of Ruprecht 106 and Terzan 7 shows that the metallicity variations are not peculiar to GCs with MPs but also characterize SP clusters.

6. Summary and Conclusions

We used multi-epoch ACS/WFC and UVIS/WFC3 images in the F275W, F336W, F438W, F606W, and F814W bands from GO 17075 (PI: Lagioia) and from the HST archive to investigate MPs in the four outer-halo GCs Arp 2, Ruprecht 106, Terzan 7, and Terzan 8. We derived high-precision stellar magnitudes, positions, and PMs by using the methods and computer programs developed by J. Anderson and colleagues (e.g., J. Anderson & I. R. King 2000; J. Anderson et al. 2006). The resulting five-band photometry is comparable to that of 58 less distant GCs studied in the recent surveys of MPs (G. Piotto et al. 2015; A. P. Milone et al. 2017), thus providing a total sample of 62 homogeneously analyzed Galactic GCs. The main results are summarized in the following:

1. We derived $\Delta_{C\,\rm F275W,F336W,F438W}$ versus $\Delta_{\rm F275W,F814W}$ ChMs to search for MPs with different light-element abundances. We find that Arp 2 and Terzan 8 host MPs, whereas Ruprecht 106 and Terzan 7 are SP clusters. This is the first evidence of simple stellar population GCs based on a ChM, and corroborates previous conclusions based on spectroscopy of nine stars of Ruprecht 106 (S. Villanova et al. 2013), photometry in the *U*, *B*, *I* bands of RGB stars in both Ruprecht 106 and Terzan 7 (A. Dotter et al. 2018; E. P. Lagioia et al. 2019a), and the HB morphology of Ruprecht 106 (A. P. Milone et al. 2014).
2. It is widely accepted that the $C_{\rm F275W,F336W,F438W}$ pseudo-color width of the RGB correlates with the average cluster metallicity. In GCs with MPs, the RGB width mostly depends on the maximum internal variation in the abundances of CNO. This color index is primarily sensitive to the nitrogen content of the stellar populations and, to a lesser extent, to variations in helium, carbon, and oxygen (e.g., A. P. Milone et al. 2015; E. P. Lagioia et al. 2019a; S. Jang et al. 2021). In addition to light-element spread, star-to-star metallicity variations can also contribute to the RGB width (e.g., A. F. Marino et al. 2019b). We find that the observed RGB widths of Arp 2

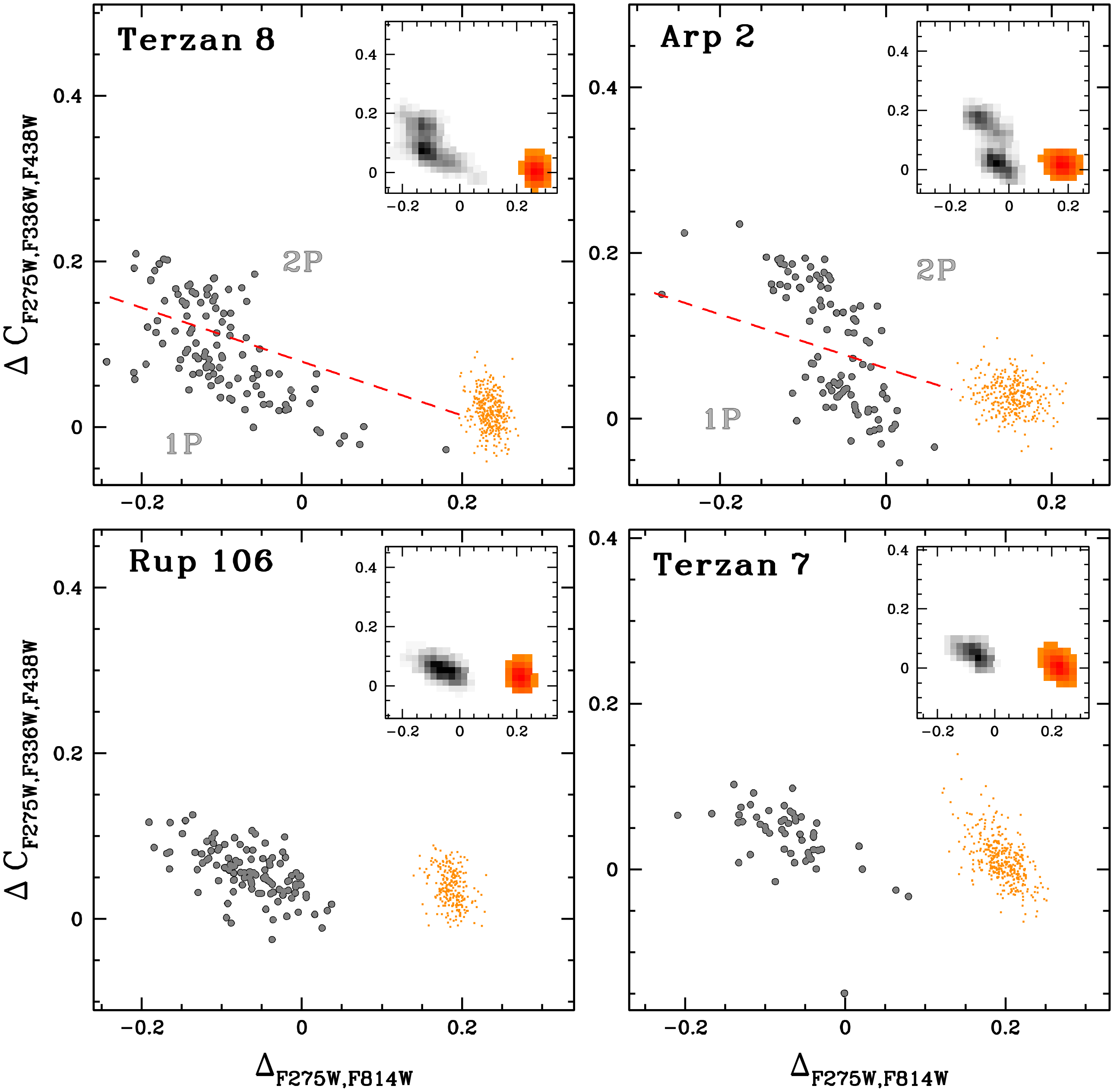

Figure 5. Chromosome maps of the RGB stars in the four target clusters, arranged as in Figure 1. In each panel, the orange points display the corresponding photometric error distribution, while the inset show the density diagram of the ChM and error distribution. The dashed line in the ChM of Terzan 8 and Arp 2 delimit the region of the ChM where 1P and 2P candidate stars lie.

and Terzan 8 follow the same trend as the bulk of Galactic GCs in the $W_{C\mathrm{F275W,F336W,F438W}}$ versus [Fe/H] diagram. On the contrary, the RGB widths of Ruprecht 106 and Terzan 7 are much narrower than those of GCs with similar [Fe/H], as expected for clusters with homogeneous abundances of light elements.

3. Previous works have suggested that a mass threshold could govern the occurrence of MPs in GCs. Based on analysis of the ChMs for 58 Galactic GCs, A. P. Milone et al. (2020) noticed that the MP GCs have masses larger than $\sim 1.5 \times 10^5\, M_\odot$. Arp 2 is the Galactic GC with the smallest initial mass ($\sim 0.9 \times 10^4\, M_\odot$) for which MPs have been detected through its ChMs. The discovery of MPs in this cluster suggests that the proposed mass threshold, if present, should be smaller than $\sim 10^5\, M_\odot$. In this context, it is worth noting that various SP Magellanic Cloud GCs have initial masses of $(1–3) \times 10^5\, M_\odot$, which are larger than those of Arp 2 and Terzan 8. This fact could indicate that, in addition to cluster mass, the GC formation environment affects the occurrence of MPs, with metal-poor GCs having a lower initial mass threshold for the formation of 2P stars (M. G. H. Krause et al. 2016; R. Huang et al. 2024). In this regard, a possible interpretation for the nonoccurrence of MPs in some GCs is that the emergence of star clusters with MPs may also depend on the environment (M. G. H. Krause et al. 2016; R. Huang et al. 2024), though it is not obvious how the environment could affect the process. An alternative explanation for the lack of MPs is that this phenomenon would only occur in stars less massive than

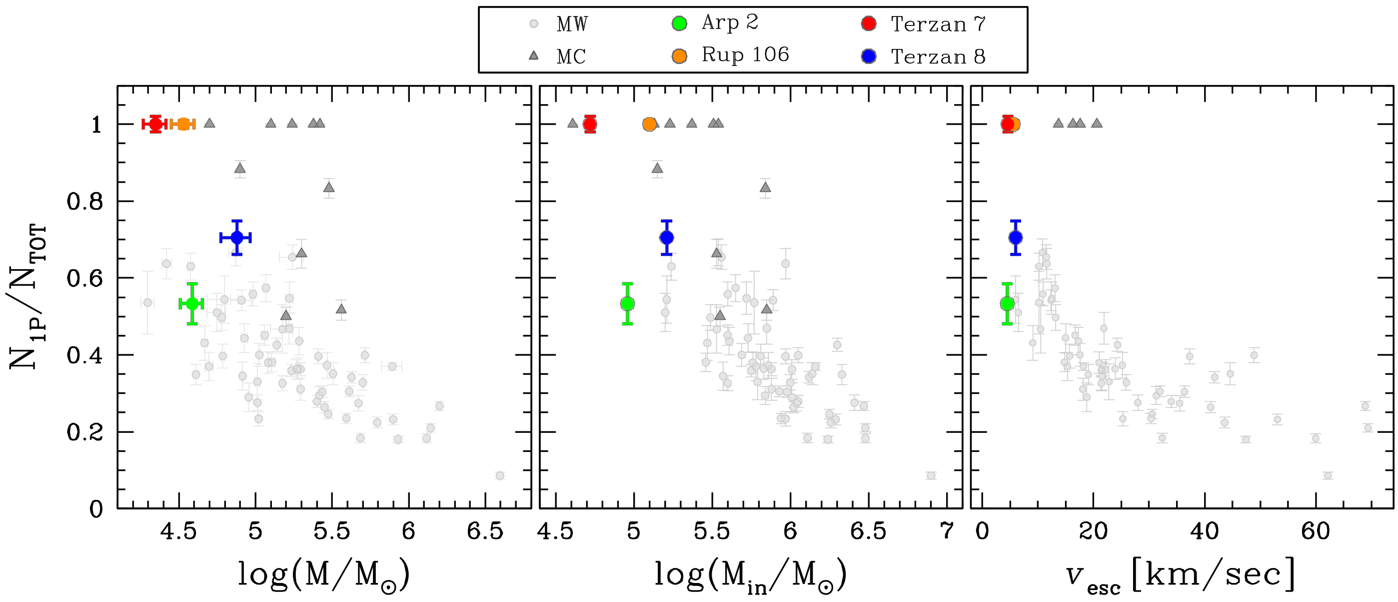

Figure 6. Fraction of 1P stars as a function of the logarithm of the GC present-day mass, initial mass, and escape velocity. The gray symbols refer to literature determinations of the 1P fractions in Milky Way and Magellanic Cloud clusters (A. P. Milone et al. 2017; E. Dondoglio et al. 2021), whereas the GCs studied in this paper are indicated with colored dots, as indicated in the legend.

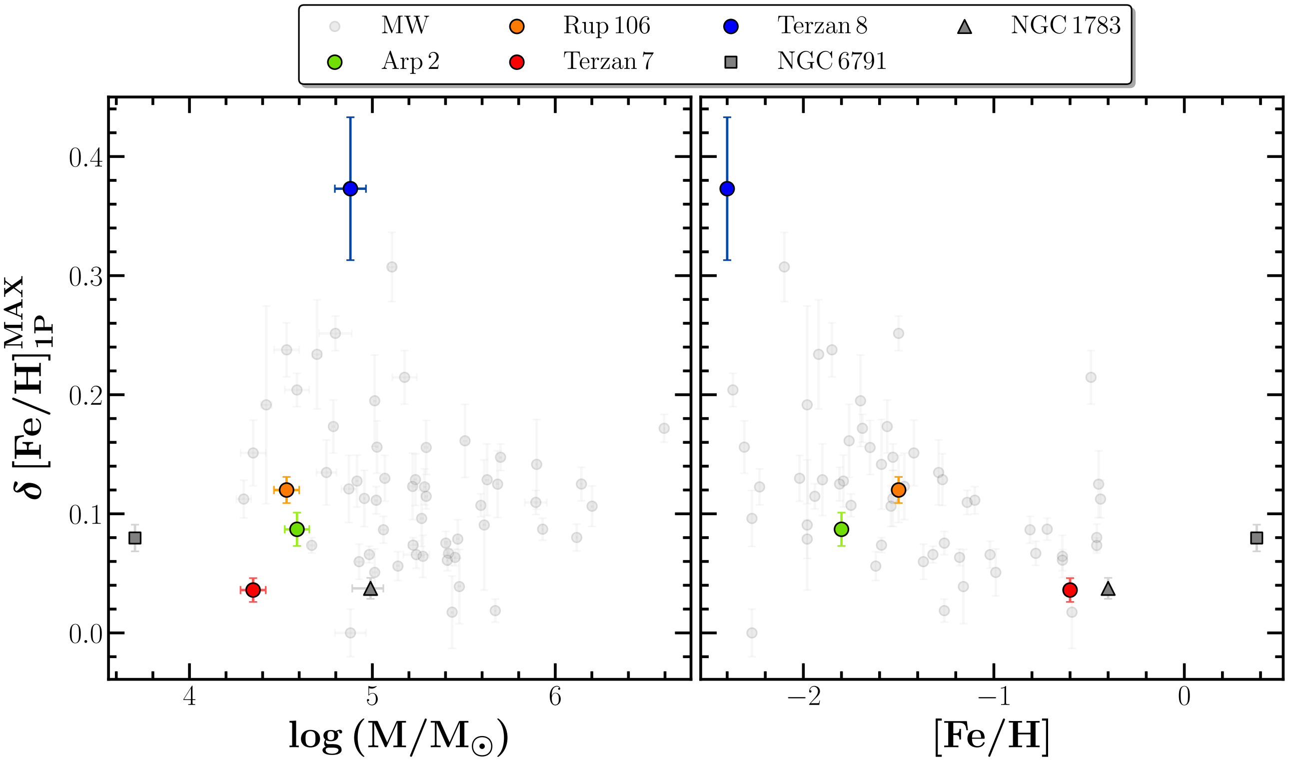

Figure 7. Maximum iron-abundance variation among 1P stars as a function of the logarithm of present-day GC mass (left) and iron abundance (right). The clusters studied in this paper are plotted with colored points as reported in the legend. The gray points indicate the GCs studied by M. V. Legnardi et al. (2022), whereas the SP star clusters NGC 6791 and NGC 1783 are represented with a square and a triangle, respectively (M. V. Legnardi et al. 2024).

$\sim$1.6 $M_\odot$ only (N. Bastian & C. Lardo 2018). In such a case, the reason for the lack of detection of 2P stars in some Magellanic Cloud GCs is that MP studies in Magellanic Cloud GCs younger than $\sim$2 Gyr are exclusively based on RGB stars.

4. We used ChMs to derive the fractions of 1P stars in Arp 2 and Terzan 8, which correspond to 53.3% ± 5.2% and 71.0% ± 4.4%, respectively. Noticeably, the Galactic GCs with MPs and large perigalactic radii ($R_{\rm peri} > 3.5$ kpc) studied in the literature tend to have higher fractions of 1P stars compared to the other Milky Way GCs. This behavior is particularly pronounced in the clusters studied in the Magellanic Cloud, where the fraction of 1P stars is even higher than in Galactic GCs

with large $R_{\rm peri}$ (M. Zennaro et al. 2019; A. P. Milone et al. 2020), thus suggesting that the fraction of 1P stars may depend on the environment. Intriguingly, while Terzan 8 clearly follows the overall trend of MW GCs, Arp 2 is a possible outlier and shares similar fractions of 1P stars as some Galactic GCs with similar masses and small $R_{\rm peri}$.

5. The 1P stars of the MP GCs Arp 2 and Terzan 8 exhibit intrinsic $m_{\rm F275W} - m_{\rm F814W}$ color spreads, which likely indicates the presence of star-to-star [Fe/H] variations of ∼0.1 and 0.3 dex, respectively. A recent study of 55 Galactic GCs with MPs by M. V. Legnardi et al. (2022) has shown that the 1P stars of virtually all clusters exhibit extended sequences in the ChM. These observations are consistent with inhomogeneous [Fe/H] abundances, ranging from less than 0.05 to ∼0.3 dex. Hence, the results for Arp 2 and Terzan 8 corroborate the evidence that metallicity variations among 1P stars are common features of GCs.
6. We found that the SP GCs Ruprecht 106 and Terzan 7 also exhibit extended 1P sequences in their ChMs, closely resembling those observed in 1P stars of MP GCs. This finding, combined with evidence of star-to-star [Fe/H] variations in the open cluster NGC 6791 and the ∼1.5 Gyr old star cluster NGC 1783 (M. V. Legnardi et al. 2024), indicates that this phenomenon is not exclusive to MP GCs but also occurs in SP GCs, open clusters, and intermediate-age massive Magellanic Cloud clusters. Although high-precision spectroscopic observations are required to definitively determine the chemical composition of these systems, star-to-star metallicity variations remain the most plausible explanation for the extended sequences observed in their ChMs.

Acknowledgments

E.P.L. acknowledges support from the "Science & Technology Champion Project" (grant No. 202005AB160002) and from the "Top Team Project" (grant No. 202305AT350002), all funded by the "Yunnan Revitalization Talent Support Program." T.Z. acknowledges funding from the European Union's Horizon 2020 research and innovation program under the Marie Skłodowska-Curie grant Agreement No. 101034319 and from the European Union—Next Generation EU. This work has received funding from "PRIN 2022 2022MMEB9W—Understanding the formation of globular clusters with their multiple stellar generations" (PI: Anna F. Marino), and from INAF Research GTO-Grant Normal RSN2-1.05.12.05.10 (ref. Anna F. Marino) of the "Bando INAF per il Finanziamento della Ricerca Fondamentale 2022."

Facilities: HST (WFC3/UVIS), HST (WFC/ACS).

ORCID iDs

E. P. Lagioia https://orcid.org/0000-0003-1713-0082
A. P. Milone https://orcid.org/0000-0001-7506-930X
M. V. Legnardi https://orcid.org/0000-0003-3153-1499
G. Cordoni https://orcid.org/0000-0002-7690-7683
E. Dondoglio https://orcid.org/0000-0001-8415-8531
A. Renzini https://orcid.org/0000-0002-7093-7355
M. Tailo https://orcid.org/0000-0002-1128-098X
T. Ziliotto https://orcid.org/0000-0001-8538-2068
M. Carlos https://orcid.org/0000-0003-1757-6666
S. Jang https://orcid.org/0000-0002-1562-7557
A. F. Marino https://orcid.org/0000-0002-1276-5487
A. Mohandasan https://orcid.org/0000-0001-5182-0330
J. Qi https://orcid.org/0009-0007-8203-7753
G. Rangwal https://orcid.org/0000-0002-6373-770X
F. Muratore https://orcid.org/0009-0003-0121-7500

References

Anderson, J., & Bedin, L. R. 2010, PASP, 122, 1035
Anderson, J., Bedin, L. R., Piotto, G., Yadav, R. S., & Bellini, A. 2006, A&A, 454, 1029
Anderson, J., & King, I. R. 2000, PASP, 112, 1360
Anderson, J., Sarajedini, A., Bedin, L. R., et al. 2008, AJ, 135, 2055
Bastian, N., Lamers, H. J. G. L. M., de Mink, S. E., et al. 2013, MNRAS, 436, 2398
Bastian, N., & Lardo, C. 2018, ARA&A, 56, 83
Baumgardt, H., & Hilker, M. 2018, MNRAS, 478, 1520
Baumgardt, H., & Vasiliev, E. 2021, MNRAS, 505, 5957
Bedin, L. R., Cassisi, S., Castelli, F., et al. 2005, MNRAS, 357, 1038
Bellazzini, M., Ferraro, F. R., & Ibata, R. 2003, AJ, 125, 188
Bellazzini, M., Ibata, R., Malhan, K., et al. 2020, A&A, 636, A107
Bellini, A., Anderson, J., & Bedin, L. R. 2011, PASP, 123, 622
Caloi, V., & D'Antona, F. 2011, MNRAS, 417, 228
Carretta, E., Bragaglia, A., Gratton, R. G., et al. 2009, A&A, 505, 117
Carretta, E., Bragaglia, A., Gratton, R. G., et al. 2014, A&A, 561, A87
Cottrell, P. L., & Da Costa, G. S. 1981, ApJL, 245, L79
D'Antona, F., Gratton, R., & Chieffi, A. 1983, MmSAI, 54, 173
D'Antona, F., Vesperini, E., D'Ercole, A., et al. 2016, MNRAS, 458, 2122
de Mink, S. E., Pols, O. R., Langer, N., & Izzard, R. G. 2009, A&A, 507, L1
Denisenkov, P. A., & Denisenkova, S. N. 1989, ATsir, 1538, 11
Denissenkov, P. A., & Hartwick, F. D. A. 2014, MNRAS, 437, L21
Dondoglio, E., Milone, A. P., Lagioia, E. P., et al. 2021, ApJ, 906, 76
Dotter, A., Milone, A. P., Conroy, C., Marino, A. F., & Sarajedini, A. 2018, ApJ, 865, L10
Dotter, A., Sarajedini, A., Anderson, J., et al. 2010, ApJ, 708, 698
Dotter, A., Sarajedini, A., & Yang, S.-C. 2008, AJ, 136, 1407
François, P. 2014, MmSAI, 85, 303
Frelijj, H., Villanova, S., Muñoz, C., & Fernández-Trincado, J. G. 2021, MNRAS, 503, 867
Gaia Collaboration, Vallenari, A., Brown, A. G. A., et al. 2023, A&A, 674, A1
Gieles, M., Charbonnel, C., Krause, M. G. H., et al. 2018, MNRAS, 478, 2461
Gilliland, R. L., Rajan, A., & Deustua, S. 2010, Instrument Science Report WFC3 2010-10
Gratton, R., Sneden, C., & Carretta, E. 2004, ARA&A, 42, 385
Gratton, R. G., Carretta, E., & Bragaglia, A. 2012, A&ARv, 20, 50
Harris, W. E. 1996, AJ, 112, 1487
Huang, R., Tang, B., Li, C., et al. 2024, SCPMA, 67, 259513
Jang, S., Milone, A. P., Lagioia, E. P., et al. 2021, ApJ, 920, 129
Jang, S., Milone, A. P., Legnardi, M. V., et al. 2022, MNRAS, 517, 5687
Kamann, S., Giesers, B., Bastian, N., et al. 2020, A&A, 635, A65
Kraft, R. P. 1994, PASP, 106, 553
Krause, M., Charbonnel, C., Decressin, T., Meynet, G., & Prantzos, N. 2013, A&A, 552, A121
Krause, M. G. H., Charbonnel, C., Bastian, N., & Diehl, R. 2016, A&A, 587, A53
Lagioia, E. P., Milone, A. P., Marino, A. F., Cordoni, G., & Tailo, M. 2019a, AJ, 158, 202
Lagioia, E. P., Milone, A. P., Marino, A. F., & Dotter, A. 2019b, ApJ, 871, 140
Lagioia, E. P., Milone, A. P., Marino, A. F., et al. 2018, MNRAS, 475, 4088
Lagioia, E. P., Milone, A. P., Marino, A. F., et al. 2021, ApJ, 910, 6
Lagioia, E. P., Milone, A. P., Stetson, P. B., et al. 2014, ApJ, 785, 81
Lardo, C., Salaris, M., Cassisi, S., & Bastian, N. 2022, A&A, 662, A117
Law, D. R., & Majewski, S. R. 2010, ApJ, 718, 1128
Lee, J.-W. 2015, ApJS, 219, 7
Legnardi, M. V., Milone, A. P., Armillotta, L., et al. 2022, MNRAS, 513, 735
Legnardi, M. V., Milone, A. P., Cordoni, G., et al. 2024, A&A, 687, A160
Lucertini, F., Monaco, L., Caffau, E., et al. 2023, A&A, 671, A137
Marino, A. F., Milone, A. P., Dondoglio, E., et al. 2023, ApJ, 958, 31
Marino, A. F., Milone, A. P., Renzini, A., et al. 2019a, MNRAS, 487, 3815
Marino, A. F., Milone, A. P., Sills, A., et al. 2019b, ApJ, 887, 91
Marino, A. F., Villanova, S., Piotto, G., et al. 2008, A&A, 490, 625
Martell, S. L., Smolinski, J. P., Beers, T. C., & Grebel, E. K. 2011, A&A, 534, A136

Martins, F., Morin, J., Charbonnel, C., Lardo, C., & Chantereau, W. 2020, A&A, 635, A52
Mehta, V. J., Milone, A. P., Casagrande, L., et al. 2025, MNRAS, 536, 1077
Milone, A. P., Bedin, L. R., Piotto, G., & Anderson, J. 2009, A&A, 497, 755
Milone, A. P., & Marino, A. F. 2022, Univ, 8, 359
Milone, A. P., Marino, A. F., Da Costa, G. S., et al. 2020, MNRAS, 491, 515
Milone, A. P., Marino, A. F., Di Criscienzo, M., et al. 2018a, MNRAS, 477, 2640
Milone, A. P., Marino, A. F., Dotter, A., et al. 2014, ApJ, 785, 21
Milone, A. P., Marino, A. F., Piotto, G., et al. 2015, MNRAS, 447, 927
Milone, A. P., Marino, A. F., Renzini, A., et al. 2018b, MNRAS, 481, 5098
Milone, A. P., Piotto, G., Bedin, L. R., et al. 2012a, ApJ, 744, 58
Milone, A. P., Piotto, G., Bedin, L. R., et al. 2012b, A&A, 540, A16
Milone, A. P., Piotto, G., Renzini, A., et al. 2017, MNRAS, 464, 3636
Mottini, M., Wallerstein, G., & McWilliam, A. 2008, AJ, 136, 614
Piotto, G., Milone, A. P., Bedin, L. R., et al. 2015, AJ, 149, 91
Pritzl, B. J., Venn, K. A., & Irwin, M. 2005, AJ, 130, 2140
Renzini, A., D'Antona, F., Cassisi, S., et al. 2015, MNRAS, 454, 4197
Renzini, A., Marino, A. F., & Milone, A. P. 2022, MNRAS, 513, 2111
Salinas, R., & Strader, J. 2015, ApJ, 809, 169
Sbordone, L., Bonifacio, P., Buonanno, R., et al. 2007, A&A, 465, 815
Shirazi, A. R., Khalaj, P., & Haghi, H. 2024, MNRAS, 531, 2563
Silverman, B. W. 1986, Monographs on Statistics and Applied Probability (London: Chapman and Hall)
Tailo, M., Milone, A. P., Lagioia, E. P., et al. 2021, MNRAS, 503, 694
Tang, B., Wang, Y., Huang, R., et al. 2021, ApJ, 908, 220
Tautvaišienė, G., Wallerstein, G., Geisler, D., Gonzalez, G., & Charbonnel, C. 2004, AJ, 127, 373
Villanova, S., Geisler, D., Carraro, G., Moni Bidin, C., & Muñoz, C. 2013, ApJ, 778, 186
Yong, D., & Grundahl, F. 2008, ApJL, 672, L29
Yong, D., Grundahl, F., Nissen, P. E., Jensen, H. R., & Lambert, D. L. 2005, A&A, 438, 875
Zennaro, M., Milone, A. P., Marino, A. F., et al. 2019, MNRAS, 487, 3239